Additive Manufacturing: Metallurgy, Cut Analysis & Porosity

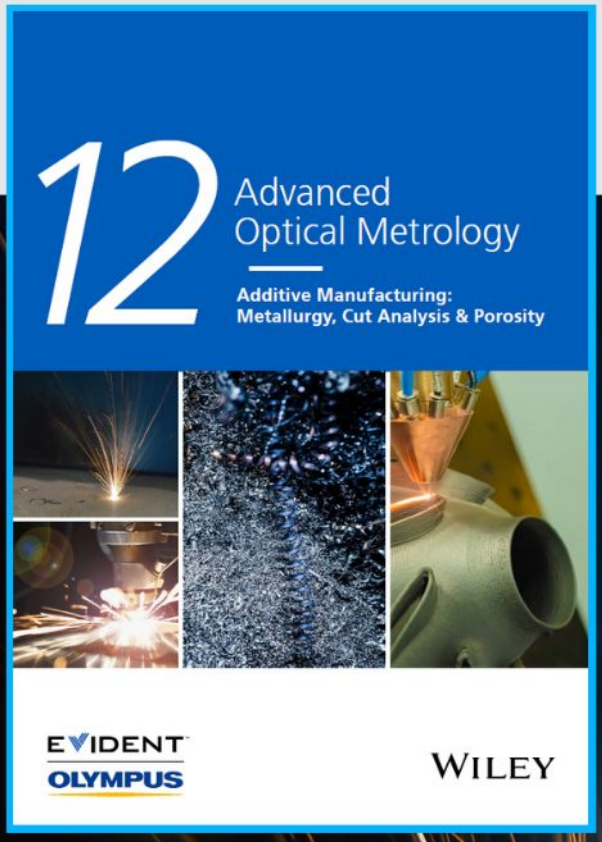

The latest eBook from Advanced Optical Metrology. Download for free.

In industry, sector after sector is moving away from conventional production methods to additive manufacturing, a technology that has been recommended for substantial research investment.

Download the latest eBook to read about the applications, trends, opportunities, and challenges around this process, and how it has been adapted to different industrial sectors.

EVIDENT
OLYMPUS

WILEY

NANO · MICRO small
www.small-journal.com

Plasmonic Nanoassemblies: Tentacles Beat Satellites for Boosting Broadband NIR Plasmon Coupling Providing a Novel Candidate for SERS and Photothermal Therapy

Priyanka Dey, Tanveer A. Tabish, Sara Mosca, Francesca Palombo, Pavel Matousek, and Nicholas Stone**

Optical theranostic applications demand near-infrared (NIR) localized surface plasmon resonance (LSPR) and maximized electric field at nanosurfaces and nanojunctions, aiding diagnosis via Raman or optoacoustic imaging, and photothermal-based therapies. To this end, multiple permutations and combinations of plasmonic nanostructures and molecular "glues" or linkers are employed to obtain nanoassemblies, such as nanobranches and core–satellite morphologies. An advanced nanoassembly morphology comprising multiple linear tentacles anchored onto a spherical core is reported here. Importantly, this core-multi-tentacle-nanoassembly (CMT) benefits from numerous plasmonic interactions between multiple 5 nm gold nanoparticles (NPs) forming each tentacle as well as tentacle to core (15 nm) coupling. This results in an intense LSPR across the "biological optical window" of 650–1100 nm. It is shown that the combined interactions are responsible for the broadband LSPR and the intense electric field, otherwise not achievable with core–satellite morphologies. Further the sub 80 nm CMTs boosted NIR-surface-enhanced Raman scattering (SERS), with detection of SERS labels at 47×10^{-9} M, as well as lower toxicity to noncancerous cell lines (human fibroblast Wi38) than observed for cancerous cell lines (human breast cancer MCF7), presents itself as an attractive candidate for use as biomedical theranostics agents.

1. Introduction

The popularity of plasmonic nanostructures stems from the ability to tune its morphology, which in turn dictates its optical properties particularly, localized surface plasmon resonance (LSPR). Researchers have invested more than two decades in developing strategies for maximizing plasmon coupling by manipulating the design of the nanostructure and interaction between nanostructures to achieve LSPR λ_{max} in specific wavelength regions. For example, UV–vis LSPR is crucial for dopant plasmonic nanostructures used in photocatalysis and solar cells to capture UV–vis photons from the sunlight;[1–3] visible region absorbance allows colorimetric-based sensing; and[4,5] metamaterials often exploit mid-infrared absorbance.[6,7] On the other hand, plasmonic nanostructures for in vivo biomedical diagnostics or for therapeutics tend to require near-infrared (NIR) LSPR,[8–13] as NIR light features the lowest absorbance by biological tissue components and thus highest penetration into tissue. Thus, NIR-active materials such as tunable plasmonic nanostructures with LSPR in the "biological optical window" of 650–1100 nm are becoming popular for biomedical theranostics applications.

Particularly, plasmonic nanoassemblies provide a gamut of possibilities, which have inspired researchers to invest years in understanding, manipulating, and controlling their formation. Constructing nanoassembly structures necessitates tuning multiple features like their morphology, nanojunction or hot-spot density, nanogap or interparticle distance, which in turn would influence the plasmon coupling and localized surface plasmon resonance (LSPR).[14] It also induces a dramatic enhancement in electric field in and around the nanojunctions resulting in intense hot-spot zones, often utilized by surface-enhanced optical spectroscopies, especially surface-enhanced Raman scattering (SERS). In addition to the importance of the interacting nanostructures and the nanoassembly morphology, the interparticle distance, i.e., the nanogap is a critical governing factor.[15–19] It has been established that sub 1 nm nanogaps allow realization of such properties.[18,20,21] Therefore, in a quest to achieve such properties, linker mediated nanoassembly formation has been

Dr. P. Dey, Dr. T. A. Tabish, Prof. F. Palombo, Prof. N. Stone
School of Physics and Astronomy
University of Exeter
Exeter EX4 4QL, UK
E-mail: n.stone@exeter.ac.uk
Dr. S. Mosca, Prof. P. Matousek
Central Laser Facility
Research Complex at Harwell
STFC Rutherford Appleton Laboratory
UK Research and Innovation
Harwell Campus, Didcot OX11 0QX, UK
E-mail: pavel.matousek@stfc.ac.uk
The ORCID identification number(s) for the author(s) of this article can be found under https://doi.org/10.1002/smll.201906780.

DOI: 10.1002/smll.201906780

extensively researched where linker molecules of sub 1 nm sizes have gained importance.

The desired NIR absorbance and intense hot-spots have been reported with complicated approaches to obtain specific nanoassembly morphologies like nanobranch and core–satellite assemblies.[22–26] Here we report for the first time a unique nanoassembly morphology comprised of multiple tentacles anchored onto a 15 nm gold core, which surpasses similar core–satellite structures in plasmon coupling and therefore their NIR absorbance (profiles) per unit gold concentration. This is made possible due to the multiple, smaller-sized 5 nm gold NPs assembled into a tentacle mimicking an elongated "bunch of grapes" structure. Such a kind of morphology features exceptional plasmonic properties, while utilizing simple "off-the-shelf" building blocks thus attractive for potential commercial applications. Additionally, we emphasize the role of the polymeric linker size and how it is not a limiting factor in achieving strong plasmon coupling.

2. Results and Discussion

2.1. Synthesis of Building Blocks

We attempted to form efficient nanoassembly morphologies, employing simple building blocks, such that they are colloidally stable and potentially scalable for future commercial applications. First, we synthesized citrate-stabilized 15 and 5 nm gold nanoparticles (AuNPs) using traditional methods of reducing chloroauric acid by sodium citrate and sodium borohydride, respectively (details of synthesis provided in the Experimental Section). The batches exhibited LSPR at

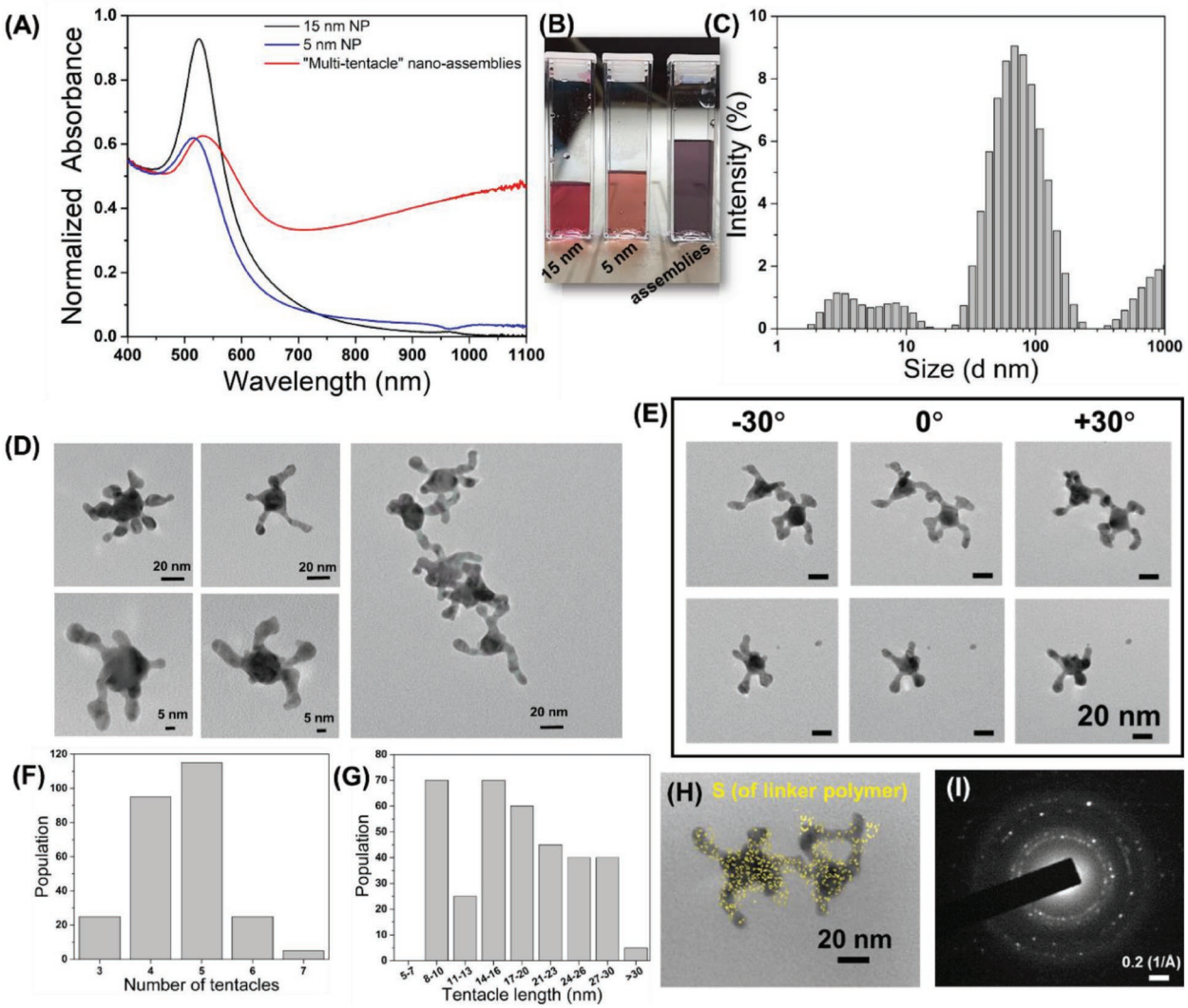

Figure 1. Physical characterization of the core multitentacular nanoassemblies. A) UV–vis spectrum of the reactants and product nanoassembly. B) Visual colloid color of the reactants and product nanoassembly. C) DLS size distribution of the nanoassembly colloid. D) Conventional TEM micrographs. E) Tilted TEM micrographs of column-wise: tilt angles of −30°, 0°, and +30° and row-wise: multiple nanoassemblies (scale bar = 20 nm). F) Statistical analysis of the number of tentacles per core of individual nanoassemblies using ImageJ on conventional TEM micrographs. G) Statistical analysis of the tentacle length using ImageJ on conventional TEM micrographs. H) TEM-EDS Mapping of sulfur (S) present in the polymeric chemical structure on nanoassemblies, and I) TEM-SAED of the nanoassemblies.

523 and 510 nm (as shown in **Figure 1**A), transmission electron microscopy (TEM) sizes of 16 ± 1 nm, 4 ± 2 nm (averaged from 90 to 100 population using ImageJ) and dynamic light scattering (DLS) median sizes of 15 and 5 nm. Linker properties and sizes have a dominating effect on the nanoassembly properties, and thus specially designed linkers including organic molecules, branched and dendrimeric polymers, DNA and DNA origami have gained attention. Furthermore, organic molecules of sub 1 nm sizes[8,27,28] have gained popularity as compared to dendrimers of 1–3 nm sizes,[29] hyperbranched polymer of 2–15 nm,[26,30,31] DNA origami of 3–10 nm,[32–34] and DNA oligomers of 8–15 nm. We here report the use of a branched flexible polymeric linker with approximate size of 2.5 nm (i.e., >1 nm) to achieve nanoassemblies. Specifically, the selected linker was a four-arm PEG5k–SH polymer (purchased from Sigma-Aldrich and used as received) with molecular weight of M_n 5000 Da, structurally imitating a four-arm star polymer with four polyethylene glycol flexible chains and a thiol end group per chain, i.e., 4 thiol end groups per polymer macromolecule. Thus the three building blocks are either easily synthesizable or commercially available (commercially available 15 and 5 nm AuNPs could also be used).

2.2. Design, Synthesis, and Understanding the Core Multitentacle Nanoassemblies

The 15 nm AuNP served as the core NP and was functionalized with the linker polymer by self-assembling it onto the NP and displacing the loosely bound citrate ions. An aliquot of 150 µL from a 10×10^{-6} M polymer aqueous solution was added to 3 mL of 15 nm AuNPs (containing ≈8.3×10^{11} NPs mL^{-1}; see the Supporting Information for more details) suggesting a theoretical availability of 3.6×10^5 polymer macromolecules/NP whereas only ≈142 polymer molecules/NP would form a monolayer of polymer in a stretched out configuration (considering the polymer footprint to be of 5 nm^2, d = 2.5 nm) and therefore was in huge excess. This thus ensured a full coverage of polymer onto the core NPs. Once equilibrium was reached by standing the solution to rest overnight, excess polymer was removed by centrifugation, and the sample was resuspended in milli-Q water. The sample featured a LSPR redshift of 2 nm and change in zeta potential from −48 mV (citrate stabilized) to −12 mV (polymer functionalized). Further increase in polymer concentration did not affect the surface charge, indicating that full coverage was reached. TEM micrographs of the polymer functionalized 15 nm AuNPs presented a polymer "halo" around each NP as observed on the holey carbon-coated TEM grid (Figure S1 in the Supporting Information). This, along with the LSPR shift and zeta potential change, confirmed the ligand exchange and polymer functionalization. A fully functionalized core NP would thus have a monolayer of densely packed polymer macromolecules; resulting in one or more thiol end groups from each polymer macromolecule being accessible for further attachment to gold surfaces.

In order to form the nanoassemblies, a huge excess of citrate-capped 5 nm NPs (say *Y*) were mixed with the above prepared polymer functionalized 15 nm core NPs (say *X*) with a volume ratio of *Y*/*X* of 6 that resulted in a NPs ratio of ≈31 (net NPs of 5 nm ÷ net NPs of 15 nm). This colloid was left overnight and later characterized by UV–vis spectroscopy. Although the absorbance profile of the product showed negligible change in the primary LSPR peak, an increase in the NIR absorbance of ≈33% of that of its LSPR (λ_{max}) was observed in the region of 650–1100 nm (see Figure S2, red curve of the Supporting Information). This sample was then centrifuged to separate the unanchored 5 nm NPs, followed by removal of the supernatant and resuspension in milli-Q water. The absorbance profile and the colloid sample color of the product nanoassembly has been shown in Figure 1A,B, along with that of the reacting building blocks. Figure 1A plots the normalized absorbance values (at 400 nm wavelength) of the different nanostructures. The absorbance value at 400 nm has typically been correlated with the gold atom [Au] concentration in the colloid.[35] Thus, the normalization (in Figure 1A and others) allow for a direct comparison of the plasmonic behavior (a functional parameter) of different nanomorphologies for identical gold concentration (a physical parameter) present in each colloid. The UV–vis–NIR spectrum of the fully formed nanoassemblies featured an LSPR primary peak at ≈540 nm with a significant increase in the broadband NIR absorbance of about 83% of that at its λ_{max} in the entire biological optical window of 650–1100 nm (see Figure 1A, red curve, main text and Figure S2, black curve, Supporting Information). Particularly, NIR absorbance of the nanoassemblies were drastically increased to about 20–30× (in the entire biological optical window) than that of the employed building blocks. Although a similar broadband NIR absorbance nature has been reported for plasmonic superlattices, they mostly range from 400 nm to 2.5 µm[36] in dimensions which often restricts in vivo use, which typically demands sub 100 nm nanostructures. Additionally, as compared to a narrow LSPR peak in the NIR region, a broadband NIR absorbance would confer the flexibility in selecting laser excitation wavelengths to execute diagnosis and therapy, making them highly versatile.

Further analysis of the morphological features of the prepared nanoassembly is shown in Figure 1C–G. The nanoassembly was characterized by a DLS median size of ≈69 nm (Figure 1C) and a TEM average size of 62 ± 4 nm measured from 87 individual nanoassembly TEM images using ImageJ (few typical TEM images have been shown in Figure 1D). Such nanoassemblies with sub 100 nm size are beneficial for in vivo diagnostic applications, as larger nanostructures would not preferentially be taken up by tumor cells by virtue of the enhanced penetration and retention (EPR) effect found in leaky tumor neovasculature. In addition, as the whole process is entirely water-based it is environment-friendly and therefore beneficial for biological applications.

In order to obtain a better understanding of the morphology of the nanoassemblies, tilted TEM was performed spanning a total angle of 60° with measurements at +30°, 0°, and −30° tilts. The tilted TEM images are shown in Figure 1E (row-wise, different nanoassemblies) at the three tilt angles (column wise). This confirms that the product nanoassemblies are unique 3D nanostructures with multiple tentacles anchored tightly onto the core and projecting in random directions. We refer to them as "core multitentacle nanoassembly" and these seem to be distinctly different from most of the morphologies cited in literature. Further analysis of the TEM micrographs, employing ImageJ and measuring ≈50–70 individual nanoassemblies, revealed that the nanoassemblies presented an average of four

to five tentacles per core (Figure 1F) with a tentacle length of ≈14–20 nm (Figure 1G), suggesting that most tentacles are longer in length than width making them resemble tentacles. On a closer look we also observed that all tentacles are ≈>8 nm in both the length and width, suggesting that neither the length nor the width was composed of a single 5 nm NP (corresponding to actual size of 4 ± 2, i.e., 2–6 nm). Additionally, they could not have been composed of 15 nm NPs. This was surprising as the freely available linker end groups would typically attach to one or two 5 nm NPs. Further in-depth analysis was thus required to ascertain if the tentacles were actually formed of 5 nm NPs linked with the polymer or if any crystal overgrowth was involved. Thus, we performed elemental mapping using energy-dispersive X-ray spectrometer (EDS)-TEM to map the sulfur of the thiol end group of polymer on nanoassemblies deposited onto a TEM grid. We noted that the sulfur (marked in yellow) (Figure 1H) was distributed both over the core NP and tentacle length suggesting that the tentacles are indeed formed of 5 nm NPs interlinked with the polymeric linker.

However, it was unclear whether the 5 nm NPs in a single tentacle were still single nanoparticles or were sintered together into a molded tentacle. To answer this, we drop casted and air-dried a high concentration of the citrate stabilized 5 nm gold NPs onto a TEM grid and used identical settings as the assemblies to acquire the images. Figure S3 (Supporting Information) show few representative images where we observe both standalone single NPs (marked with green circle) and aggregates (formed when drying, marked with red circle). The image contrast of the 5 nm gold NPs is low when compared to 15 nm gold NPs and therefore it is understandable if the periphery of overlaid NPs are visually less pronounced in 5 nm aggregates. It is also important to mention that we still observe single NPs sitting close to each other without being sintered into one. Thus although there have been reports of TEM-induced sintering of gold NPs,[37] it seems less likely that the nanoassemblies are formed of sintered 5 nm gold NPs, rather suggesting that their overlap makes it difficult to visualize their individual surfaces. We further analyzed the nanoassemblies using selected area electron diffraction selected-area electron diffraction (SAED)-TEM (Figure 1) to determine whether crystal growth could have occurred as a result of rearrangement or sintering.[38,39] We observed ring patterns consistent with polycrystalline spherical AuNPs corresponding to diffraction rings of 111, 200, 220, and 311 plane.[40,41] The most prominent ring of the low energy uniform facet of 111 confirms that the nanoassemblies are composed of the octahedral facet of single nanoparticles. The other 200, 220, and 311 reflections also correlate to facets of trapezohedron-type structures present in smaller fractions in pseudospherical nanoparticles. The absence of 100 and 110 facet confirms the absence of any rod-like or cube-like structures.[42–44] The above observation thus ruled out the likelihood of any further crystal growth in the nanoassembly morphology and is suggestive of a more elongated "bunch of grapes"-like tentacle morphology assembled of multiple 5 nm NPs.

The above data suggest the formation of core multitentacle nanoassemblies with 15 nm as the core and multiple 5 nm NPs combining to form each tentacle. The flexible ester bonds of polyethylene glycol branches of the linker makes it feasible for one polymeric linker to anchor one to three 5 nm NPs. The importance of the polymer flexibility on interparticle distance of the core–satellite nanoassemblies has also been pointed out by Rossner et al.[21] Importantly, the polymeric linker featuring a DLS average size of 2.5 ± 1.5 (i.e., 1–4) nm (see Figure S4 in the Supporting Information) creates a scenario of size overlap with some population of the 5 nm NP (i.e., 2–6 nm). The average polymer footprint is ≈5 nm^2 (2.5 nm diameter) with a range of 0.8–12 nm^2 (1–4 nm diameter) projecting onto a 5 nm NP having an average surface area of 80 nm^2 (a range of 12–113 nm^2 due to NP diameter of 2–6 nm). The steric hindrance of close packing of thiol end groups onto the high curvature of 5 nm NP, in addition to the polymer–NP size and footprint overlap, might hinder anchoring of multiple end groups onto one NP. In contrast, there is an increased probability for the polymer to bind to two or more 5 nm NPs also due to the availability of excess 5 nm NPs ($Y/X = 31$). These therefore allow for multiple anchoring aiding the formation of multitentacles.

In order to verify this, we reacted the 5 nm NPs with the polymeric linker (in absence of the core 15 nm) and observed that the 5 nm NPs assemble together forming tentacular structures without being able to observe a clear periphery of the individual 5 nm NPs (similar to what was observed for nanoassemblies) comprising the tentacular nanoassemblies (see Figure S5 in the Supporting Information). It must also be noted that such tentacle nanoassemblies presented a single peak LSPR at 525 nm and some NIR absorbance, but is devoid of a strong NIR absorbance as observed for core multitentacle assemblies. Thus the plasmon coupling between the 5 nm NPs forming only the tentacles cannot be the sole cause of the broadband NIR absorbance of the core multitentacle assemblies. When the 5 nm NPs (in absence of the core) and the polymer linker interacts with each other, the 5 nm NPs arrange themselves into elongated tentacle-like nanostructures. Both the TEM and the plasmon response (Figure S5 in the Supporting Information) suggest a low interparticle distance, as otherwise negligible plasmon coupling would be observed in a scenario of 5 nm NPs assembled with interparticle distance of say, 2–3 nm or more. This along with the flexibility of the polymeric chain suggests that the 5 nm NPs in the core multitentacle nanoassemblies are very close to each other, contributing to the plasmon coupling. These tentacles in the nanoassemblies exhibit two specific features. First, they are arranged onto the cores in a random orientation which makes the core multitentacle nanoassembly polarization independent, where the probability of one or more tentacles being aligned with the polarization mode is high. This thus provides plasmon coupling from single or multiple tentacles (each tentacle behaving similar to nanochains) without the restricted requirement of the nanochain being oriented in parallel to the light polarization. This thus boosts plasmon coupling leading to NIR absorbance. Furthermore, Figure 1F,G suggests that the multitentacle nanoassemblies are formed in a range of tentacle sizes and tentacle density (onto the core). This though indicates a higher deviation within the assembly morphology but on the other hand the multiple length of the tentacles (like nanochains of various lengths) provides multiple longitudinal LSPR peak positions which thereby, culminates into a broadened plasmon peak in the NIR. The developed core multitentacle morphology and its inherent structural properties thus allows utilization

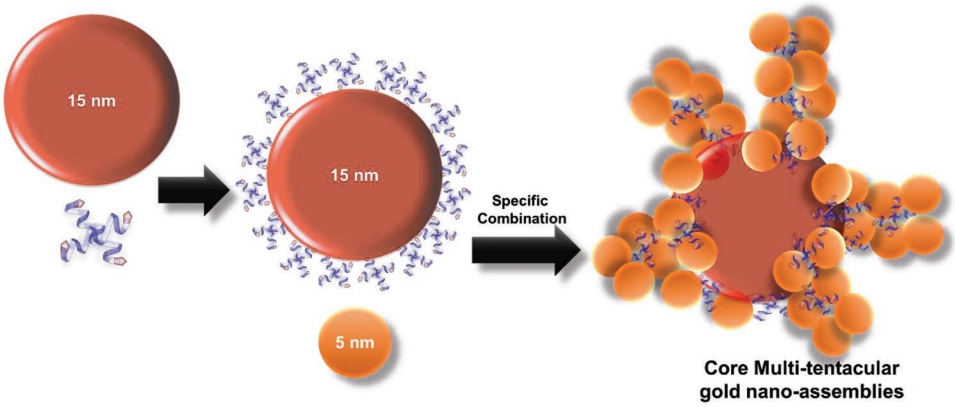

Figure 2. Cartoon representation of the formation steps of core multitentacle nanoassembly.

of all the above factors leading to the resultant increased broadband NIR plasmon response throughout the "biological optical window." This also justifies the superiority of the developed core multitentacular morphology when compared to individual tentacles. LSPR in the NIR region has been reported for multibranch linear nanoassemblies,[45] and hence suggests the importance and contribution of the multiple tentacles of the developed nanoassembly morphology toward NIR broadband absorbance. Furthermore, as the anchored polymer is in dynamic equilibrium with the gold surface, deattachment, and reattachment can possibly lead to linker molecules migrating and anchoring onto 5 nm NPs.

The schematic in **Figure 2** show the formation of such unique core multitentacular morphologies. We conclude that the multiarm polymer linker when functionalized onto the core 15 nm NPs mimics a tightly packed conformation providing a high polymer surface coverage. This high polymer density when interacting with the 5 nm NPs, due to dynamic equilibrium of polymer anchoring onto gold surface via thiol, has a tendency to deattach from the 15 nm core and reattach to the 5 nm NPs. Furthermore, as a certain population of the small 5 nm NP batch size and the polymer linker size are similar they interact in a very specific manner and allow one 4-arm polymer macromolecule to attach to both multiple 5 nm NPs forming an "elongated bunch of grapes" type tentacle structure, as well as participate in attaching one or two 5 nm NPs of one end of the tentacle with the core. As a result of the high excess of the 5 nm NPs with respect to the core NPs, multiple tentacle like structures form and are attached to the core, resulting in a core multitentacle nanoassembly. Four to six tentacles are typically observed which are spatially randomly distributed onto the core and the number of tentacles formed is probably a contribution of both a fixed excess of 5 nm NPs and the steric hindrance provided by the citrate on the 5 nm NPs. Such developed notable 3D morphologies are near-isotropic due to the random arrangement of tentacles on the core. This would thus suggest minimal dependence on polarization direction for absorbance and SERS behavior similar to nanobranched assemblies, as opposed to strong polarization dependency of anisotropic gold nanorods and linear nanochain assemblies. This behavior is especially important for in vivo applications where the orientation of the nanostructures in the biological media cannot be controlled.

2.3. LSPR Profile as a Function of Reactant Ratios

As the reactant-specific combination seems crucial in the development of the unique morphologies, we investigated different regimes of reactant ratios to shed more light into the assembly formation process. Ratios of number of reacting NPs of polymer functionalized 15 nm NP (denoted by *X*) and citrate stabilized 5 nm NP (*Y*) were studied. Near-equal NP ratios, i.e., $Y/X = 1.3$, as well as excess of *Y*, i.e., $Y/X = 5$ were prepared using similar methodologies as the previous one, which employed a great excess of *Y*, i.e., $Y/X = 31$. The three ratios yielded categorically different nanoassembly morphologies with distinctly different absorbance profiles as shown in **Figure 3**A–C. As a control, citrate stabilized 15 and 5 nm NPs were mixed in absence of the linker. The control sample presented a LSPR peak at 514 nm, as shown in Figure 1C (black spectrum), indicating that no assembly occurs in absence of the linker polymer. Employing a near-equal ratio of both ($Y/X = 1.3$) resulted in a nanoassembly with few 5 nm NPs anchored onto the core 15 nm leading to a core–satellite nanoassembly morphology with 5 nm satellites sparsely positioned on the surface of the core (Figure 3B, 1st row). The UV–vis spectrum of the core–satellite morphology (Figure 3C, pink spectrum) exhibits an LSPR peak at 534 nm with negligible NIR absorbance. This is due to the poor plasmon coupling between *X*–*Y* and low *Y* density, along with the wider nanogap due to the polymer size separating them. On the other hand, using an excess of *Y* ($Y/X = 5$), a 15 nm core densely covered with 5 nm satellites visually imitating a core–shell type morphology (Figure 3B, mid row) is observed. Figure 3C red spectrum shows the LSPR red-shifted to 557 nm, suggesting improved plasmon coupling due to the presence of higher numbers of 5 nm NPs. Distinctly different nanoassembly morphologies were thus obtained as a function of Y/X and thereby confirm the importance of the specific reactant ratios employed. The contribution of the plasmon coupling and absorbance in the "biological optical window" (650–1100 nm) of the different nanoassembly morphologies can be well realized in Figure 3D where we spectrally subtract the UV–vis of the specific assembly from that of the control, i.e., analyze the differential absorbance. Upon comparison to core–satellite and core–shell nanoassemblies, core multitentacle ones feature a significant increase in absorbance beyond

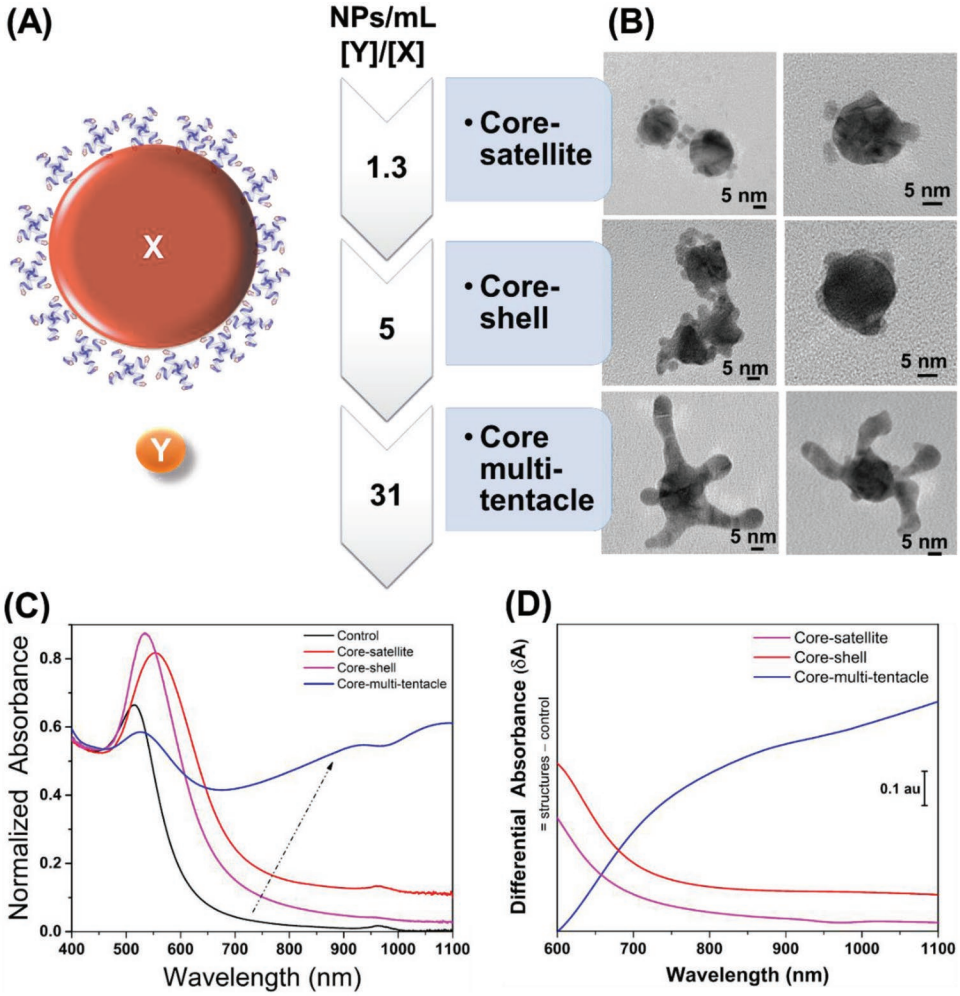

Figure 3. Effect of reactant ratios *X* and *Y*. A) Graphical representation of the reactant ratios in number of NPs and their corresponding nanoassembly morphologies formed along with their respective B) TEM micrographs (scale bar = 5 nm) and C) UV–vis spectrum normalized at 400 nm, and D) differential absorbance (δA) of their normalized absorbance of the assemblies and that of the control (as shown in (C)).

600 nm, suggesting the importance of this novel nanoassembly morphology over and above the well-studied core–satellite ones. This trend is also due to the significantly increased plasmon coupling between the *Y*–*Y* NPs, otherwise not available in the core–satellite or core–shell. Furthermore, although the polymer linker is a relatively large macromolecule (>1 nm), the flexibility of the polymer chains and multiple anchoring end groups allow for much closer packing of *Y*–*Y*, which in turn aids in reducing the gap of *X*–*Y*. This also thus suggest that the requirement of a sub 1 nm linker molecule may not be the primary factor when designing linkers.

2.4. SERS of Multitentacle Nanoassmeblies

The SERS performance was studied for the core multitentacle nanoassemblies and as they absorbed significantly in the broad NIR "biological optical window" region, a more relevant laser excitation for in vivo diagnostics was used, i.e., 830 nm laser line. 2-Quinolinethiol (QTH) was employed as the SERS label and functionalized via the thiol end group onto the gold and the respective colloid samples filled in quartz cuvettes were studied. Although ideally a high concentration of label would provide better signal and hence be efficient as a tracking agent for diagnostics, the leaching out of the label to the surrounding cellular matrix causing toxicity is a noted concern hindering its real-life applications. Thus, we explored the potential of the nanoassemblies in providing detectable SERS signals (i.e., signal to noise ratio, SNR > 2) in a wide range of concentrations. **Figure 4** spectrum i (background subtracted) demonstrates that we do not observe any signal from unlabeled core multitentacle nanoassemblies. This is due to the polyethylene glycol polymer linker featuring low Raman scattering cross-section, which also indicates that upon labeling them with SERS labels there would not be any Raman signal interference from the polymer. With significantly lower label concentration of the order of nM, it becomes essential to position them at hot-spots to be able to detect them. This was attempted by employing a prelabeling methodology which has been reported by Dey et al.[46] where the label molecule is incorporated during the nanoassembly formation and has been shown to improve the SERS signal intensities when compared with typical

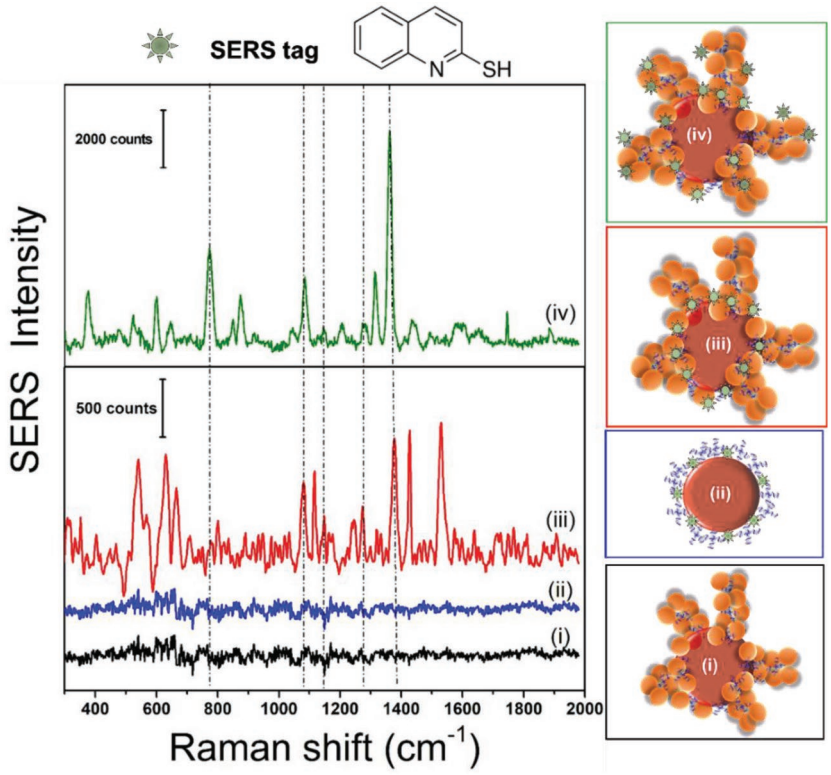

Figure 4. SERS spectrum (background subtracted for i–iii, no smoothing performed) of core multitentacle nanoassemblies measured with 830 nm laser line. Comparison of core, assemblies, and prelabeled assemblies with QTH as the SERS label i) assemblies no label ([QTH] = 0 M), ii) core labeled ([QTH] = 4.76×10^{-8} M), iii) QTH prelabeled assemblies ([QTH] = 4.76×10^{-8} M) [accumulation = 60 s], iv) assemblies postlabeled with QTH ([QTH] = 1.7×10^{-7} M) [accumulation = 50 s], along with their cartoon representations of the morphologies in inset.

postlabeling methodology (i.e., label added after nanoassembly formation). This was achieved by incorporating QTH, after the 15 nm core NP was functionalized with the polymer and before the addition of the 5 nm NPs (see the Experimental Section for preparation details), thereby guiding most of the QTH molecules to position themselves at the core surface and around the core-tentacle juncture. Figure 4A shows a comparison of the nanoassembly, labeled core NP and multitentacular assembly formed from the labeled core, i.e., a prelabeled nanoassembly. Both DLS data (median size = 68 nm) and UV–vis plots confirmed that the prelabeled assemblies were similar to the unlabeled assemblies in physical properties. Polymer functionalized core with QTH (spectrum ii) was compared to nanoassemblies prelabeled with QTH (spectrum iii) in Figure 4 both having identical concentration of QTH of 4.76×10^{-8} M, i.e., 47×10^{-9} M. Spectrum (iii) in Figure 4 shows peaks of QTH at 634, 667, 1083, 1115, 1363, 1425, and 1542 cm^{-1}.[47] The signature peak of QTH at 1363 cm^{-1} assigned to the aromatic C–C stretching, ν(CC), is prominent. Upon comparison of spectrum (ii) and (iii), it becomes evident that hot-spots created due to assembly formation makes the nM label concentration readily detectable in nanoassemblies although it remains undetectable for the core-label sample. Thus, experimentally we can detect with high SNR a significantly low concentration of 47×10^{-9} M (QTH) with the unique nanoassembly structures, suggesting a lower limit of detection (LOD) than 47×10^{-9} M (4.7×10^{-8} M) for the assemblies. When comparing this with popular SERS tags like rhodamine 6G (R6G), reports suggest experimental LOD of 10^{-6} M with nanostructured Ag–Au bimetallic surfaces.[41] Another example reporting a complicated gold–SERS label–silver nanorattle structure deposited as films inside micropipettes for SERS detection of methyl parathion featured experimental LOD of 10^{-6} M and calculated a theoretical LOD (from calibration curves) to be 68×10^{-9} M (6.8×10^{-8} M).[48] A recent review[49] suggests that most designed nanostructures allow detection of medium-high Raman cross-section molecules (labels) in the concentration range of 10^{-5} to 10^{-7} M, and detection of signal below that is quite challenging. Typically higher signal enhancement and potentially detection of below 10^{-8} M is observed for nanostars (of sizes 50–200 nm) and lowest for spherical nanoparticles (especially < 30 nm), hence the core multitentacle nanoassemblies comprised of 5 and 15 nm NPs provides a dramatic boost to the SERS signals allowing detection of 47×10^{-9} M concentrations, without compromising on the size restrictions for in vivo use.

In contrast, we also studied the more general postlabeling methodology where we incorporated the QTH onto formed nanoassemblies. As higher concentrations of QTH could not be used for prelabeled strategies due to its effect on destabilizing the core NP, we studied higher QTH concentrations for postlabeled ones, i.e., QTH added after nanoassembly formation. In that case, a QTH concentration of 1.7×10^{-7} M (0.17×10^{-6} M) was easily detectable with a high SNR as shown in Figure 4 spectrum (iv). The spectrum presented peaks at 375, 598, 772, 877, 1085, 1315, 1363, and 1441 cm^{-1}. The signature peaks at 1363 and 772 cm^{-1} assigned to the aromatic ν(CC) and ring breathing mode are prominent. Upon comparison of the pre- and postlabeled ones (marked with dotted lines in Figure 4), it becomes apparent that different signature peaks become noticeable in different labeling methods which might be attributed to the resulting orientation of the molecule in the different scenarios positioning specific chemical bonds closer or farther to the gold surface and hence yielding respectively altered signal enhancements. We thus can conclude that the prepared nanoassemblies are intensely SERS-active.

2.5. Multilabel SERS and Cell Toxicity Behavior, Promising Features of the Multitentacle Nanoassmeblies

Additionally, another SERS label biphenylthiol (BPT) was also studied at higher concentrations in the μM to mM range (as shown in Figure S6 in the Supporting Information). We observed the signature peaks at 1580, 1278, 1074, 877, 473, and

287 cm^{-1}, whose signal intensities increased with increase in added BPT concentration (in postlabeling methodology), demonstrating the high surface area of the assemblies available for anchoring functional molecules. Overall, we can conclude that core multitentacle nanoassembly aid in amplifying SERS signals, when compared with core satellites of the same base units, allowing detection of multiple SERS labels in the concentration range of nM to mM. Furthermore, we have investigated the cellular viability of the prepared core multitentacle nanoassemblies and compared their behavior in a noncancerous human fibroblast cell line Wi38 to that in a human breast cancer cell line MCF7 (see subsection and Figure S7 in the Supporting Information), with concentrations of 10–50 μg mL^{-1} used. None of the AuNPs concentrations tested were found to induce toxicity in Wi3-8 cells, although concentrations of NPs at 30 and 50 μg mL^{-1} considerably induced toxicity in MCF7 cells. In other words, the multitentacle nanoassemblies exhibited higher toxicity toward human cancerous cell line, while being biocompatible toward human noncancerous cell line. This seems promising and needs further detailed investigation to fully understand the behavior (a study which is ongoing in our lab). This may be due to the different proteome profiles, morphological characteristics, and genetic mutations of the two cell lines. This suggests that the synthesized core multitentacle nanoassemblies not only provide significantly high plasmon coupling and a broadband NIR absorbance in the full range of "biological optical window," but also demonstrated high SERS signal amplification and significantly good biocompatibility—features that when combined could transform into a potential efficient SERS theranostic agent.

3. Conclusions

In summary, we have demonstrated a simple methodology to prepare gold nanoassemblies with a distinct 3D morphology of multiple tentacles anchored onto a core. The uniqueness of our approach is the use of off-the-shelf type reactants such as AuNPs (15 and 5 nm) and a commercially available polymeric linker, without involving elaborate linker or nanoparticle synthesis. Importantly, the nanoassemblies exhibited significant broadband NIR absorbance in addition to visible absorbance, making them highly suitable for biomedical diagnostic and tracking applications in the biological optical window of 650–1100 nm. The nanoassembly size of ≈70 nm comprised of nontoxic gold and polyethylene glycol linkers in aqueous media, featuring good colloidal stability. We investigated the 3D nanomorphology and deduced that an average of 4–5 tentacles, each tentacle formed of multiple 5 nm NPs, were anchored to one 15 nm NP core. This helped coin the term core multitentacle nanoassemblies. We were also able to demonstrate that the flexibility of the employed polymeric linker although of a mean size of 2.5 nm (DLS) resulted in such a unique morphology. This thereafter emphasized that linkers need not be sub 1 nm for maximizing plasmon coupling and boosting NIR absorbance. Finally, we demonstrated that the morphology was highly dependent on the ratios between interacting NPs, and by altering these distinctly different morphologies like core–satellite, core–shell, and core multitentacle could be realized. Among all such morphologies, only the core multitentacle assemblies provided the much desired broadband NIR absorbance and thus proved itself more efficient than its core–satellite counterparts. The NIR-SERS behavior of the multitentacle assemblies labeled with different SERS labels was studied using 830 nm laser excitation, which provided detectable signals in the wide dynamic range of nM–mM. The developed nanoassemblies were also studied for their cellular response and was observed to be biocompatible for normal (noncancerous) human cell line while being toxic for human cancerous cell line. Thus we have successfully demonstrated the importance and potential of the developed core multitentacle nanoassemblies as novel medical theranostics agents.

4. Experimental Section

Nanoparticle Synthesis: 15 nm citrate-stabilized gold NPs was synthesized using the Turkevich's method[50,51] by using 0.3×10^{-3} M of 100 mL chloroauric acid solution. This was brought to boil and 2.6 mL of 1% (w/v) of trisodium citrate was added to it. The solution was boiled for 10 min under vigorous stirring changing its color from yellow to black to wine red. The colloid exhibited a LSPR at 523 nm, [Au] concentration of 0.289×10^{-3} M and NP concentration of 8.3×10^{11} NPs mL^{-1} (calculated from absorbance at 450 nm from the equation reported by Hais et al.[52]). The 5 nm NPs were prepared by reducing 0.3×10^{-3} M of 100 mL chloroauric acid solution at room temperature by adding 1.2 mL of 0.1 M freshly prepared ice-cold sodium borohydride in the presence of 4 mL of 1% (w/v) sodium citrate acting as the stabilizer. The solution was stirred at room temperature for 10 min which resulted in orangeish red colloid. The colloid exhibited a LSPR at 510 nm, [Au] concentration of 0.237×10^{-3} M and NP concentration of 4.3×10^{12} NPs mL^{-1}.

Synthesis of Core Multitentacle Nanoassemblies: A stock polymer solution (4-arm PEG-SH, 5000 Da) of 10×10^{-6} M was prepared by dissolving in milli-Q water. 150 μL of this polymer stock solution was added to 3 mL of the 15 nm citrate-stabilized gold NP under stirring. After thorough mixing by vortexing, it was left overnight at room temperature to complete ligand exchange. One or more of the 4-thiol groups of each polymer macromolecule would replace the loosely bound citrate ions of the NPs. This sample was later centrifuged at 14 000 rpm for 10 min and the clear supernatant containing excess unanchored polymer was removed. The pellet was resuspended in milli-Q water to the original volume and sonicated. The sample was analyzed with UV–vis spectroscopy and TEM. Figure S1 (Supporting Information) shows a TEM image of a NP with a halo of the polymer around it. This sample exhibited a LSPR shift of ≈2 nm due to the polymer anchoring onto the gold NP surface, but no NIR plasmon coupling was observed, as shown in Figure S2 (Supporting Information) blue spectrum. The polymer-functionalized 15 nm NP (referred to as "X" in the main text) was thereafter reacted with 18 mL of citrate-stabilized 5 nm NP batch (referred to as "Y" in the main text). The volume ratio of Y/X was 6 whereas, the ratio of the net number of NPs interacting, i.e., *Y*/*X* was 1.3. The colloid was left overnight and characterized by UV–vis spectroscopy. The sample demonstrated NIR absorbance due to strong plasmon coupling, in addition to a LSPR peak in the visible region, as shown in Figure S2 (Supporting Information) red "*X*+*Y*" spectrum. This colloid was then centrifuged at 14 000 rpm for 10 min. The supernatant was not clear and consisted of unanchored 5 nm NPs which was confirmed by studying its UV–vis spectrum. The pellet was resuspended with milli-Q water to make up a volume of 1.5 mL in total, which was sonicated and vortexed for 30–60 s each. The product nanoassembly colloid exhibited extended strong broadband NIR absorbance, as shown in Figure S2 (Supporting Information) black "nanoassemblies" spectrum.

Synthesis of Other Nanoassemblies: The above procedure was repeated with different volume ratios ranging from 6 to 0.25 for *Y*/*X*. A *Y*/*X* volume ratio of 1 correlated to number of NPs ratio of 1.3 and yielded

core–satellite nanoassemblies, whereas, a volume ratio of 4, i.e., a NPs ratio of 5 yielded a core–shell assembly morphology. The core was formed from the 15 nm *X* NP and the satellite, shell, or tentacles comprised of the 5 nm NPs.

Preparation of SERS Labeled Nanostructures: 150 µL of 10×10^{-6} M polymer stock solution was added to 3 mL of the 15 nm citrate-stabilized gold NP under stirring. This was followed by addition of 150 µL of 1×10^{-6} M of QTH solution (1:1 of ethanol:water) under stirring. After thorough mixing by vortexing, it was left overnight at room temperature. This was used as the QTH-labeled core NP. It was then employed to prepare the multiple-tentacle nanoassemblies identically as their unlabeled counterparts, which was referred to as QTH prelabeled core multitentacle nanoassemblies. In order to prepare postlabeled QTH assemblies, 150 µL of 1×10^{-6} M of QTH stock solution was added to 700 µL of nanoassemblies resulting in a net calculated 1.7×10^{-7} M (0.17×10^{-6} M) QTH. After stirring and equilibrating for 1 h, NIR-SERS of the samples was studied by exciting the colloid with 830 nm laser line. In order to prepare three postlabeled BPT assemblies: 10, 100, and 200 µL of 1×10^{-3} M BPT stock solution was added to 700 µL of nanoassemblies. After stirring and equilibrating for 1 h the samples were studied for NIR-SERS providing a net BPT concentration of 1.4×10^{-5}, 1.25×10^{-4}, and 2.22×10^{-4} M, respectively.

Instruments: UV–vis Spectroscopy: UV–vis spectra were acquired using an Evolution Array UV–Visible spectrophotometer in the range of 400–1100 nm with a 1 cm path length cell with baseline correction.

Dynamic Light Scattering: DLS measurements were performed using a Malvern Zetasizer Ultra running DTS software and a 4 mW He–Ne laser at 633 nm. Analysis was performed at an angle of 90° and a constant temperature of 25 °C. Dilute particle concentrations were used to ensure that multiple scattering and particle–particle interactions could be considered to be negligible. Disposable cuvettes of 1 cm pathlength was employed for size measurements, whereas, surface charge zeta potential measurements were performed in a capillary folded disposable cuvette. Three repeats of each were collected and an average and median value obtained from them.

Transmission Electron Microscopy: A JEOL 2100 TEM was used to study the NP morphologies on 200 mesh holey C-coated copper grids at 100 kV. As-prepared hybrid samples were diluted 100-fold and deposited on TEM grids so as to minimize the drying artifacts. The sizes were determined using ImageJ software by measuring ≈50–70 individual assemblies per sample. Additionally, EDS and SAED was measured on the TEM grid with the same sample on which TEM was performed. EDS was performed with an Oxford Instrument X-MAXN EDS detector, it allows chemical analysis of features as small as a few nanometers. The SAED measurements were performed at 200 kV.

Raman Spectroscopy: SERS spectra were recorded in the spectral range of 200–2000 cm^{-1} with a Renishaw model InVia micro-Raman spectrometer equipped with 830 nm excitation from a diode laser, a single diffraction grating, and an electrically cooled CCD detector. The laser power was ≈30 mW at the sample. Accumulations from 10 to 60 s were used for various measurements. Low-volume quartz cuvettes were used as sample holders and all SERS spectrum obtained from colloidal samples.

Supporting Information

Supporting Information is available from the Wiley Online Library or from the author.

Acknowledgements

The work was supported by "RaNT" EPSRC Programme Grant (EP/R020965/1).

Conflict of Interest

The authors declare no conflict of interest.

Keywords

branched polymers, broadband NIR absorbance, cell toxicity, core–satellites, plasmonic nanoassemblies, surface-enhanced Raman scattering (SERS)

Received: November 21, 2019
Revised: December 27, 2019
Published online: January 30, 2020

[1] E. B. Creel, E. R. Corson, J. Eichhorn, R. Kostecki, J. J. Urban, B. D. McCloskey, *ACS Energy Lett.* **2019**, *4*, 1098.
[2] M. J. Kale, T. Avanesian, P. Christopher, *ACS Catal.* **2014**, *4*, 116.
[3] S. Linic, P. Christopher, D. B. Ingram, *Nat. Mater.* **2011**, *10*, 911.
[4] M. Li, S. K. Cushing, N. Wu, *Analyst* **2015**, *140*, 386.
[5] H. I. Peng, B. L. Miller, *Analyst* **2011**, *136*, 436.
[6] H. Zhu, F. Yi, E. Cubukcu, *Nat. Photonics* **2016**, *10*, 709.
[7] J. Y. Ou, E. Plum, J. Zhang, N. I. Zheludev, *Adv. Mater.* **2016**, *28*, 729.
[8] S. Ye, G. Marston, J. R. Mclaughlan, D. O. Sigle, N. Ingram, S. Freear, J. J. Baumberg, R. J. Bushby, A. F. Markham, K. Critchley, P. L. Coletta, S. D. Evans, *Adv. Funct. Mater.* **2015**, *25*, 2117.
[9] V. Pansare, S. Hejazi, W. Faenza, R. K. Prud'homme, *Chem. Mater.* **2012**, *24*, 812.
[10] B. Jang, J. Y. Park, C. H. Tung, I. H. Kim, Y. Choi, *ACS Nano* **2011**, *5*, 1086.
[11] H. Kim, K. Chung, S. Lee, D. H. Kim, H. Lee, *Wiley Interdiscip. Rev.: Nanomed. Nanobiotechnol.* **2016**, *8*, 23.
[12] E. B. Dickerson, E. C. Dreaden, X. Huang, I. H. El-Sayed, H. Chu, S. Pushpanketh, J. F. McDonald, M. A. El-Sayed, *Cancer Lett.* **2008**, *269*, 57.
[13] X. Chen, Q. Zhang, J. Li, M. Yang, N. Zhao, F. J. Xu, *ACS Nano* **2018**, *12*, 5646.
[14] A. Klinkova, R. M. Choueiri, E. Kumacheva, *Chem. Soc. Rev.* **2014**, *43*, 3976.
[15] R. Jin, *Angew. Chem., Int. Ed.* **2010**, *49*, 2826.
[16] M. Moskovits, *Phys. Chem. Chem. Phys.* **2013**, *15*, 5301.
[17] T. Vo-dinh, Y. Liu, A. M. Fales, H. Ngo, H. Wang, J. K. Register, H. Yuan, S. J. Norton, G. D. Griffin, *Wiley Interdiscip. Rev.: Nanomed. Nanobiotechnol.* **2015**, *7*, 17.
[18] D. Lee, S. Yoon, *J. Phys. Chem. C* **2016**, *120*, 20642.
[19] J. M. Romo-Herrera, R. A. Alvarez-Puebla, L. M. Liz-Marzan, *Nanoscale* **2011**, *3*, 1304.
[20] H. Cha, D. Lee, J. H. Yoon, S. Yoon, *J. Colloid Interface Sci.* **2016**, *464*, 18.
[21] C. Rossner, Q. Tang, O. Glatter, M. Müller, P. Vana, *Langmuir* **2017**, *33*, 2017.
[22] H. Deng, F. Dai, G. Ma, X. Zhang, *Adv. Mater.* **2015**, *27*, 3645.
[23] J. Pan, L. Zhang, S. Zhang, Z. Shi, X. Wang, S. Song, H. Zhang, *ACS Appl. Nano Mater.* **2019**, *2*, 1516.
[24] A. Poletti, G. Fracasso, G. Conti, R. Pilot, V. Amendola, *Nanoscale* **2015**, *7*, 13702.
[25] Z. Yang, J. Song, Y. Dai, J. Chen, F. Wang, L. Lin, Y. Liu, F. Zhang, *Theranostics* **2017**, *7*, 2177.
[26] P. Dey, I. Blakey, K. J. Thurecht, P. M. Fredericks, *Langmuir* **2013**, *29*, 525.
[27] S. T. Jones, R. W. Taylor, R. Esteban, E. K. Abo-Hamed, P. H. Bomans, N. A. Sommerdijk, J. Aizpurua, J. J. Baumberg, O. A. Scherman, *Small* **2014**, *10*, 4298.
[28] N. Hüsken, R. W. Taylor, D. Zigah, J.-C. Taveau, O. Lambert, O. A. Scherman, J. J. Baumberg, A. Kuhn, *Nano Lett.* **2013**, *13*, 6016.
[29] Q. Chen, H. Wang, H. Liu, S. Wen, C. Peng, M. Shen, G. Zhang, X. Shi, *Anal. Chem.* **2015**, *87*, 3949.

[30] P. Dey, S. Zhu, K. J. Thurecht, P. M. Fredericks, I. Blakey, *J. Mater. Chem. B* **2014**, *2*, 2827.
[31] P. Dey, I. Blakey, K. J. Thurecht, P. M. Fredericks, *Langmuir* **2014**, *30*, 2249.
[32] V. V Thacker, L. O. Herrmann, D. O. Sigle, T. Zhang, T. Liedl, J. J. Baumberg, U. F. Keyser, *Nat. Commun.* **2014**, *5*, 3448.
[33] C. Shen, X. Lan, X. Lu, T. A. Meyer, W. Ni, Y. Ke, Q. Wang, *J. Am. Chem. Soc.* **2016**, *138*, 1764.
[34] P. Kuhler, E. M. Roller, R. Schreiber, T. Liedl, T. Lohmuller, J. Feldmann, *Nano Lett.* **2014**, *14*, 2914.
[35] T. Hendel, M. Wuithschick, F. Kettemann, A. Birnbaum, K. Rademann, J. Polte, *Anal. Chem.* **2014**, *86*, 11115.
[36] N. Kwon, H. Oh, R. Kim, A. Sinha, J. Kim, J. Shin, J. W. M. Chon, B. Lim, *Nano Lett.* **2018**, *18*, 5927.
[37] Y. Chen, R. E. Palmer, J. P. Wilcoxon, *Langmuir* **2006**, *22*, 2851.
[38] P. Eirini, Goudeli, E. Sotiris, *Adv. Mater.* **2016**, *62*, 405.
[39] M. H. Magnusson, K. Deppert, J. Malm, J. Bovin, L. Samuelson, *J. Nanopart. Res.* **1999**, *1*, 243.
[40] M. F. Lengke, M. E. Fleet, G. Southam, *Langmuir* **2006**, *22*, 2780.
[41] Y. Guan, H. Su, C. Yang, L. Wu, S. Chen, J. Gu, W. Zhang, D. Zhang, *Sci. Rep.* **2018**, *8*, 1.
[42] H. Zhang, C. Guan, N. Song, Y. Zhang, H. Liu, J. Fang, *Phys. Chem. Chem. Phys.* **2018**, *20*, 3571.
[43] Z. Quan, Y. Wang, J. Fang, *Acc. Chem. Res.* **2013**, *46*, 191.
[44] M. Zhu, B. Lei, F. Ren, P. Chen, Y. Shen, B. Guan, Y. Du, T. Li, M. Liu, *Sci. Rep.* **2014**, *4*, 5259.
[45] P. Ginzburg, N. Berkovitch, A. Nevet, I. Shor, M. Orenstein, *Nano Lett.* **2011**, *11*, 2329.
[46] P. Dey, K. J. Thurecht, P. M. Fredericks, I. Blakey, *Appl. Spectrosocpy* **2019**, *73*, 1428.
[47] P. Dey, W. Olds, I. Blakey, K. J. Thurecht, E. L. Izake, P. M. Fredericks, *J. Raman Spectrosc.* **2013**, *44*, 1659.
[48] W. Fang, X. Zhang, Y. Chen, L. Wan, W. Huang, A. Shen, J. Hu, *Anal. Chem.* **2015**, *87*, 9217.
[49] J. Reguera, J. Langer, D. Jiménez de Aberasturi, L. M. Liz-Marzán, *Chem. Soc. Rev.* **2017**, *46*, 3866.
[50] J. Turkevich, P. C. Stevenson, J. Hillie, *Discuss. Faraday Soc.* **1951**, *11*, 55.
[51] M. Brust, J. Fink, D. Bethell, D. J. Schiffrin, C. Kiely, *J. Chem. Soc., Chem. Commun.* **1995**, *16*, 1655.
[52] W. Haiss, N. T. K. Thanh, J. Aveyard, D. G. Fernig, *Anal. Chem.* **2008**, *80*, 6620.